Applicability of a drift-flux model of aerosol deposition in a test tunnel and an indoor heritage environment

Josep Grau-Bové [⋆], Matija Strlič [⋆], Luca Mazzei [⋆⋆]

[⋆] *Institute for Sustainable Heritage, The Bartlett School of Graduate Studies, UCL, 14 Upper Woburn Place, London WC1H 0NN, UK*

[⋆⋆] *Department of Chemical Engineering, UCL, Torrington Place, London WC1E 7JE, UK*

Primary corresponding author Luca Mazzei (l.mazzei@ucl.ac.uk)

Secondary corresponding author Josep Grau-Bove (josep.grau.bove@ucl.ac.uk)

Abstract

Near-wall turbulence associated with air flows parallel to walls can promote aerosol deposition. In indoor environments, where this kind of flow is frequently present, this results in local deposition gradients near ventilation inlets and outlets. This phenomenon is of special interest to the heritage field, which is often concerned about the spatial distribution of deposition and its links to environmental management. In this paper we investigate the capability of a drift-flux model of particulate matter deposition to describe this mechanism. This model has often been validated using decay rates of particulate matter concentration; however, in several indoor applications the interest is not in concentration but in the spatial distribution of the deposition flux. To test the model, we use untreated atmospheric aerosols in two different cases: an experimental tunnel designed to induce near-wall velocity gradients and an actual indoor room with various ventilation regimes. Both systems exhibit significantly inhomogeneous deposition distributions. While the first system is operated under controlled laboratory conditions, the second yields data collected in-situ during a six-month monitoring campaign. In either case the model reproduces the experimental values with enough accuracy to allow understanding how the environment behaves. This work confirms the usability of the drift-flux approach as an analysis tool for particle deposition in complex environments in a wide range of geometries.

Keywords: Deposition, Aerosol, CFD, Drift-Flux.

---

1 Introduction

Particulate matter (PM) deposition constitutes one of the most challenging concerns in heritage preservation. Moreover, the prevailing conditions under which heritage is presented to the public pose special challenges to PM deposition models. During the last decades, the development of mathematical models of deposition has been driven by interest in the respiratory system [1] and the behavior of PM indoors [2]. Recently, many museums and historical buildings have become increasingly concerned about PM as a carrier of pollutants and a soiling agent [3], which has triggered a rise in the use of monitoring and sampling [4].

Heritage managers confront several problems related to particle deposition, which PM deposition models can help address. Firstly, heritage institutions have long been interested in identifying which surfaces receive the largest amount of particles, and why [5]. Consequently, their interest is frequently not in well-mixed rooms, but in rooms where inhomogeneous deposition profiles develop. These profiles are often caused by differences of near-wall velocity, induced by local sources of air movement related to mechanical ventilation. A typical issue faced by heritage institutions would be, for example, to identify which walls are safe to display the most vulnerable objects.

Another concern in several heritage environments is the dynamic and short-term evolution of particle concentration. Most of these environments are not isolated from the outdoor environment, and often particles penetrate indoors through the windows or the main doors [6]. A common problem is to understand the evolution of concentration indoors once a visitor has opened the main gate of a room and to know how far particles will spread and what their maximum concentration will be.

In the literature there are many mathematical models that can enable this prediction. One of the most well-tested approaches to the simulation of aerosol dispersion and deposition is the “drift-flux” family of models, which describe the motion of suspensions of particles in air in an Eulerian framework [7]. The equations for particle movement are typically coupled with expressions for the deposition flux, such as the three-layer model proposed by Lai and Nazaroff [8], which has been adopted as a wall treatment in many implementations of the drift-flux model [9, 10].

This approach has later been refined and validated [11, 12]. More general drift-flux models have been proposed that incorporate sources of particle drift different from gravity in order to include other deposition mechanisms. Zhao et al. [13] presented an improved drift-flux model that incorporated thermophoresis and that was easily extendable to other mechanisms. Turbophoresis was included by Zhao and Wu [14], and Ramechecandane et al. [15] incorporated the drift originated by an inhomogeneous electric field, thus demonstrating that the drift-flux model may be easily adapted to account for the physics relevant to specific applications.

It has been shown that drift-flux models are well capable of simulating deposition in multi-room indoor environments with mechanical ventilation [16]. Some of the cases investigated include empty rooms and systems of connected rooms [17, 18], offices with occupants [19, 20, 21], indoor spaces with furniture [22, 23] and airplane cabins [24]. Recent advancements in the simulation of indoor aerosol dispersion are moving beyond the initial drift-flux model combined with the Reynolds-Averaged Navier Stokes (RANS) approach to model turbulence. For instance, Karadimou and Markatos [25] presented a new discretization scheme that eliminates the numerical diffusion associated with the convection terms of the conservation equations. Two-way coupling schemes for very dilute systems have been introduced [26]. Lattice Boltzmann models have also been applied for the prediction of deposition indoors with promising results [27, 28]. Regarding the fluid velocity field, Large Eddy Simulation (LES) is increasingly used for indoor air quality applications [29], even if RANS is still a popular choice [30, 31]. Comparisons between the different approaches generally indicate that LES performs better in particle deposition studies but presents a higher computational cost [32, 33]. It has been demonstrated, however, that the simulation of very dilute aerosols can be achieved with the simpler models, such as the drift-flux approach, both in RANS and LES turbulence schemes [26].

The research by Zhao and Wu [34] indicates the importance of the spatial distribution of concentration in indoor deposition studies. Few other investigations have, however, analyzed the ability of the drift-flux approach to reflect the spatial variability of deposition due to variations in near-wall flows. Deposition is usually assessed using the decay rate of the particle concentration [18, 22, 35, 36, 21, 37, 24], which reflects the *overall* deposition. In some cases, CFD models have been validated using methods which are sensitive to the spatial variation of particle deposition. For instance, Wong et al. [38] measured the deposition of bioaerosols in multiple locations on the floor of a scaled chamber, King et al. [39] measured the distribution of bioaerosol in a hospital room, while Xi and Longest [40] measured the distribution of deposition in the respiratory system. In this work, we follow a similar approach, measuring the number of particles deposited on different surfaces.

The main focus of this work is environments in which inhomogeneous deposition is dictated by local differences in shear flow. This is of direct practical interest to heritage environments, in which deposition is frequently monitored to assess its spatial variation. However, given the uncertainty associated with field data, controlled laboratory experiments become necessary. The design of our experimental setup is informed by previous research on similar problems. The drift-flux model has been validated experimentally in a wide range of geometries and velocities, from small lab setups to large indoor environments. The authors of the drift-flux model in the form we implement it, that is, Lai and collaborators, used their approach to simulate various geometries, from a tunnel with a square section of 0.15 m and 0.5 m in length [41] to an experimental chamber with a volume of 0.13 m^3 [22], a larger chamber of 1.8 m^3 [42] and full scale rooms [43]. With this research, we intend to confirm the applicability of the drift-flux approach to situations in which the spatial distribution of deposition is dictated by inhomogeneous air flows, and particularly air flows approximately parallel to walls. Following a similar approach to that of Lai and collaborators, we developed controlled experiments with air flows parallel to walls in a laboratory wind tunnel and also in full scale rooms – in fact a real museum showroom – in a range of particle size and flow conditions similar to those present in the experiments of Lai et al. [41]. Another aim of this work is exploring the ability of the drift-flux model to reflect the short-term dynamical evolution of concentration after a burst of particles is introduced in the system.

2 Multiphase fluid-dynamic model

The system we are modeling is a multiphase flow in which air transports very diluted small particles. Particle size is such that the Stokes number St is vanishingly small (in our system, for a particle with diameter d_s of $0.5\,\mu$m, St $\sim 10^{-5}$), and therefore we assume that particles have negligible inertia. According to Marchisio and Fox [44], two indicators need to be considered to assess the applicability of the one-way coupling modeling strategy: the volume fraction of solid ϕ and the phase-mass ratio $\varphi \equiv (\phi\rho_s)/(\alpha\rho_e)$, where α and ρ_e are the volume fraction and density of the fluid, respectively, while ρ_s is the solid density. A system is defined to be very dilute when both $\phi \ll 1$ and $\varphi \ll 1$. In our case, a particle density of $\rho_s \sim 1000$ kg/m^3, a particle diameter of $d_s \sim 1$ μm and a concentration of $c \sim 10^5$ $1/\text{cm}^3$ lead to $\phi \sim 10^{-2}$ and $\varphi \sim 10^{-5}$. We can assume, therefore, that one-way coupling is applicable and that collisions between particles are so infrequent that particle coagulation can be ignored.

Given these assumptions, particles are modeled as a continuous phase (Eulerian approach) and their number density is treated as a scalar advected at the same velocity as the fluid phase. The velocity field is calculated using the Reynolds Averaged Navier-Stokes equations with different turbulence models as detailed in Section 5. The equations reported in the following sections are implemented in the commercial software Ansys Fluent 12. The computational details of the numerical solution are given in Section 6. The transport equation for the particle phase can be expressed as:

$$\partial_t c = -\,\partial_{\boldsymbol{x}} \cdot c(\boldsymbol{u} + \boldsymbol{v}) + \partial_{\boldsymbol{x}} \cdot (\mathscr{D} + \mathscr{D}_t)\partial_{\boldsymbol{x}} c \tag{2.1}$$

where c is the aerosol number concentration, $\mathscr{D}$ and $\mathscr{D}_t$ are the Brownian and turbulent diffusivities of the aerosol, respectively, $\boldsymbol{u}$ is the velocity of the fluid phase, and $\boldsymbol{v}$ is the settling velocity of the particles, whose direction is parallel to that of the gravitational field. We employ the drift-flux model as presented by Chen et al. [9], which uses the near-wall functions proposed by Lai and Nazaroff [8] with corrections by Parker et al. [45]. This approach includes the contribution of air movement, gravity and turbulence on the deposition flux. Since the walls are in thermal equilibrium with the air, we do not consider thermophoresis as a particle deposition mechanism, even if the drift-flux approach has been extended to include it by Zhao et al. [13]. We solve the customary fluid-phase linear momentum balance equation (ignoring the presence of the particles) to determine $\boldsymbol{u}$. The estimation of $\mathscr{D}_t$ is discussed in Section 4. We obtain the magnitude v of the particle settling velocity from the calculation of the Reynolds number Re and Archimedes number Ar of a single particle suspended in the fluid [46]:

$$v = \frac{\mu \mathrm{Re}}{\rho_e d_s} \tag{2.2}$$

$$\mathrm{Re} = [-3.809 + (3.809^2 + 1.832\mathrm{Ar}^{0.5})^{0.5}]^2 \tag{2.3}$$

$$\mathrm{Ar} \equiv \frac{g d_s^3 \rho_e (\rho_s - \rho_e)}{\mu^2} \tag{2.4}$$

where g is the gravity and μ is the viscosity of the fluid. The Brownian diffusivity of the aerosol is estimated with the following expression Reist [47]:

$$\mathscr{D} = C\left(\frac{k_B T}{3\pi d_s \mu}\right) \tag{2.5}$$

where T is the fluid temperature, k_B is the Boltzmann constant and C is the Cunningham slip correction factor, given by the following equation:

$$C = 1 + \frac{2\lambda}{d_s}\left[A_1 + A_2 \exp\left(-\frac{A_3 d_s}{\lambda}\right)\right] \quad \text{with} \quad \lambda \equiv \frac{k_B T}{\sqrt{2}\pi p d_s^2} \tag{2.6}$$

where $A_1 = 1.257$, $A_2 = 0.400$ and $A_3 = 0.55$, and where λ and p denote the mean free path and the fluid pressure, respectively.

3 Boundary conditions

Equation 2.1 is a second-order differential equation that requires a boundary condition on all the boundaries of the domain. At the inlet, we provide a fixed concentration value (Dirichlet condition), while at the outlet we set the concentration gradient to zero (Neumann condition). At the walls of the domain, we provide the boundary condition by specifying the total particle flux toward the wall, *i.e.*, the deposition flux.

Very near the wall, a one-dimensional particle concentration gradient forms, creating a concentration boundary layer. This gradient generates a diffusive particle flux that can be expressed with a Fick's law in which the diffusion coefficient is given by the sum of the Brownian and turbulent diffusivities. The overall deposition flux at the wall J is given by the sum of this diffusive flux and of the convective flux due to the gravity-induced particle settling. Thus, we can write:

$$J = -\,(\mathscr{D} + \mathscr{D}_t)\partial_n c + (\boldsymbol{v} \cdot \boldsymbol{n})c \tag{3.1}$$

where $\partial_n c$ is the partial derivative of the aerosol concentration in the direction normal to the wall and $\boldsymbol{n}$ is the unit vector normal to the wall and pointing to the exterior of the domain; therefore $\boldsymbol{v} \cdot \boldsymbol{n}$ is the component of the settling velocity normal to the wall. One of the strengths of the drift-flux approach is that any additional velocities relevant to a particular system, such as electrical mobility drift velocity or thermophoretic velocity, can be easily added to the convective terms of Equations 2.1 and 3.1.

We calculate the value of J with the expression derived by Lai and Nazaroff [8]:

$$J = v_d c_p \quad \text{with} \quad v_d = \frac{\boldsymbol{v} \cdot \boldsymbol{n}}{1 - \exp[-\,(I/u^\star)\boldsymbol{v} \cdot \boldsymbol{n}]} \tag{3.2}$$

where v_d denotes the deposition velocity and where c_p is the particle concentration in the first mesh point p off the wall (this point falls within the inertial sublayer of the turbulent boundary layer). If a boundary wall is vertical, so that $\boldsymbol{v} \cdot \boldsymbol{n} = 0$, the expression for v_d reduces to:

$$\text{for } \boldsymbol{v} \cdot \boldsymbol{n} = 0 \quad : \quad v_d = \lim_{x \to 0} \frac{x}{1 - \exp[-\,(I/u^\star)x]} = \lim_{x \to 0} \frac{x}{1 - 1 + (I/u^\star)x} = u^\star/I \tag{3.3}$$

In Equations 3.2 and 3.3, $u^\star$ is the friction velocity, defined as $(\tau_w/\rho)^{1/2}$, where τ_w is the wall shear stress, while I is a function of the Schmidt number Sc given by the expressions reported below, as derived by Lai and Nazaroff [8]:

$$\text{Sc} = \nu/\mathscr{D} \quad ; \quad I = [3.64 \cdot \text{Sc}^{2/3}(a - b) + 39] \tag{3.4}$$

$$a = 0.5\ln\left[\frac{(10.92\cdot \mathrm{Sc}^{-1/3}+4.3)^3}{\mathrm{Sc}^{-1}+0.0609}\right] + \sqrt{3}\tan^{-1}\left[\frac{8.6-10.92\cdot \mathrm{Sc}^{-1/3}}{\sqrt{3}\cdot 10.92\cdot \mathrm{Sc}^{-1/3}}\right] \tag{3.5}$$

$$b = 0.5\ln\left[\frac{(10.92\cdot \mathrm{Sc}^{-1/3}+r^+)^3}{\mathrm{Sc}^{-1}+7.669\cdot 10^{-4}\cdot r^+}\right] + \sqrt{3}\,\tan^{-1}\left[\frac{2r^+-10.92\cdot \mathrm{Sc}^{-1/3}}{\sqrt{3}\cdot 10.92\cdot \mathrm{Sc}^{-1/3}}\right] \tag{3.6}$$

$$r^+ = d_s u^\star (2\nu)^{-1} \tag{3.7}$$

where ν is the kinematic viscosity of the fluid. To determine the value of the wall shear stress, we used wall functions, adopting two approaches: the standard and the enhanced wall function treatments. The former is based on the log-law of the wall proposed by Launder and Spalding [48], which holds in the inertial (or fully turbulent) sublayer of the turbulent boundary layer. This equation reads:

$$\tau_w = \rho_e (u_\tau^\star)^2 (u_p/u_p^\star) \tag{3.8}$$

$$u_\tau^\star \equiv C_\mu^{1/4} k_p^{1/2} \quad , \quad u_p^\star = u_\tau^\star\Big[(1/\kappa)\ln y_p^\star + B\Big] \quad , \quad y_p^\star \equiv (u_\tau^\star/\nu) y_p \tag{3.9}$$

where κ is the von Karman constant (0.4187), B and C_μ are empirical constants (B = 5.449, C_μ = 0.09), p is the first mesh point off the wall, u_p is the mean fluid velocity at point p, k_p is the turbulence kinetic energy at point p and y_p is the distance from point p to the wall. When the enhanced wall treatment is used in Fluent, τ_w is computed with an alternative expression; we do not report the expression here, referring to the literature for brevity [49, 50].

3.1 On the outlet boundary condition

The need of a boundary condition at the outlet of the system poses a conceptual problem, because in most practical applications the particle concentration or flux at the outlet are unknown. To inspect this issue, let us consider the tunnel system and define the following dimensionless variables:

$$\bar{\boldsymbol{x}} \equiv \boldsymbol{x}/x_c \quad , \quad \bar{t} \equiv t/t_c \quad , \quad \bar{c} \equiv c/c_c \quad , \quad \bar{\boldsymbol{u}} \equiv \boldsymbol{u}/u_c \quad , \quad \bar{\boldsymbol{v}} \equiv \boldsymbol{v}/u_c \tag{3.10}$$

where x_c is the characteristic length over which the dependent variables change significantly, taken as the height of the tunnel, c_c is the inlet particle concentration and u_c is the mean bulk fluid velocity. The time scale can be left undefined. Introducing these dimensionless variables in Equation 2.1 yields:

$$\partial_t c = -\,\{t_c u_c/x_c\}\partial_{\boldsymbol{x}}\cdot c(\boldsymbol{u}+\boldsymbol{v}) + \{t_c(\mathscr{D}+\mathscr{D}_t)/x_c^2\}\partial_{\boldsymbol{x}}\cdot\partial_{\boldsymbol{x}} c \tag{3.11}$$

where, to simplify the notation, we have not used different symbols to denote the dimensionless variables. Because t_c appears in both bracketed terms, the relative importance of these is unaffected by the time scale value and is given by the Péclet number:

$$\text{Pé} \equiv \frac{u_c x_c}{\mathscr{D} + \mathscr{D}_t} \tag{3.12}$$

Here to simplify the arguments reported below we have assumed that $\mathscr{D} + \mathscr{D}_t$ is constant (this assumption, however, has not been used in the simulations). We know that the characteristic dimension of the tunnel is order 0.1 m and that the fluid velocity is order 1 m/s. A representative value for the turbulent diffusivity in the tunnel is 10^{-4} m^2/s, as shown later in Figure 7e. Given these estimates, we can expect that Pé $\sim 10^3$. Because the Péclet number is far larger than unity, and the partial derivatives of the scaled variables have order unity, we conclude that in the bulk – where the scales employed are correct – diffusion is negligible. Neglecting this term, however, reduces Equation 3.11 to a first-order differential equation.

This reasoning tells us that near some boundaries (those where we had to assign boundary conditions and can no longer do so in the simplified problem) the simplified equation is incorrectly scaled. In these regions, the length scale characterizing the gradients must be far shorter, so that diffusion is not negligible. This also means that within these region concentration varies sharply, as it occurs in boundary layers. One of these sharp gradients is present at the tunnel exit. The outlet boundary condition affects the concentration profile (but not the overall flux) within this layer, but its influence in the remaining part of the domain is minimal [51, 52]. Hence, if we are interested only in the bulk solution, the outlet boundary condition does not play a critical role.

4 Eddy diffusivity

When modeling fluid-particle flows with an Eulerian approach, the concept of particle eddy diffusivity arises as a means to describe the particle motion due to the presence of turbulent eddies. An inertia-less particle is transported by the fluid at all the scales of turbulent motion and consequently has a turbulent diffusivity $\mathscr{D}_t$ identical to the turbulent diffusivity of the fluid ν_t. Generally speaking, the order of magnitude of $\mathscr{D}_t$ for atmospheric aerosols is considered to be equal to the turbulent diffusivity of the carrier fluid [53], and it has been suggested that this is a valid assumption for relaxation times under 0.1 seconds based on various experimental results [8].

To determine if this assumption is reasonable in our particular case, and to ensure that the laboratory and field experiments are comparable in this respect, we propose to use the inertial parameter proposed by

Schnell et al. [54], which describes the ability of a particle to respond to the fluid motion in an eddy. This parameter is defined in terms of the relaxation time τ, the characteristic turbulence root mean square of the fluctuating velocity u_{rms} and the integral length scale ℓ characterizing the turbulent velocity field:

$$K_{pt} = \frac{\tau u_{\mathrm{rms}}}{\ell} \quad \text{with} \quad \tau = \frac{\rho_s d_s^2}{18\mu} \tag{4.1}$$

For very small values of K_{pt}, the ratio $\mathscr{D}_t/\nu_t \approx 1$. We obtained the range of values of u_{rms} characteristic of our system from a dynamic simulation adopting the RNG $k-\varepsilon$ turbulence model. In the contours of u_{rms} displayed in Figure 7f, we can see that its order of magnitude is 1 m/s. The integral scale of turbulence is of the order $(C_\mu^{3/4} k^{3/2})/\varepsilon$, where $C_\mu = 0.09$, k is the turbulent kinetic energy and ε is the dissipation rate of k [55]. These parameters are related to the RNG $k-\varepsilon$ turbulence model. In wall bounded flows, ℓ is sometimes considered to be similar to the hydraulic diameter [56]. In the case of the tunnel, both definitions provide the same order of magnitude, which is $\ell \sim 0.1$ m. With these estimates, K_{pt} is considerably smaller than unity in the tunnel flow, as it has also been observed for the room flow. Therefore, henceforth we assume that $\mathscr{D}_t = \nu_t$. The value of ν_t in the boundary layer is calculated following Chen et al. [9], while that in the bulk is provided by the turbulence model.

5 Turbulence models

The model described above requires the use of a submodel able to estimate ν_t. Several models available in Fluent fit this description. In the $k-\varepsilon$ model $\nu_t = (C_\mu k^2)/\varepsilon$. The application of the renormalization group theory in the RNG $k-\varepsilon$ version of the model results in an identical expression for the turbulent viscosity, the only difference being in the value ascribed to the constant C_μ, which in this case is equal to 0.0845. In the $k-\omega$ model $\nu_t = (\alpha k)/\omega$, where α is a function of k and ω that corrects the turbulent diffusivity at low Reynolds numbers [for its expression, we refer to FLUENT [57]]. Lastly, in the Spalart-Allmaras model $\nu_t = \bar{\nu}_t f_v$, where $\bar{\nu}_t$ is a scalar field governed by a transport equation and f_v is a viscous damping function [for further details, we refer to FLUENT [57]]. As the simulations must predict the near-wall turbulence accurately, we use the models of turbulence with both standard and enhanced wall functions.

6 Computational setup

The simulations have been carried out in Ansys Fluent 12. The model has been implemented through an User Defined Function (UDF). A structured grid was used for all simulations. The grid size was chosen

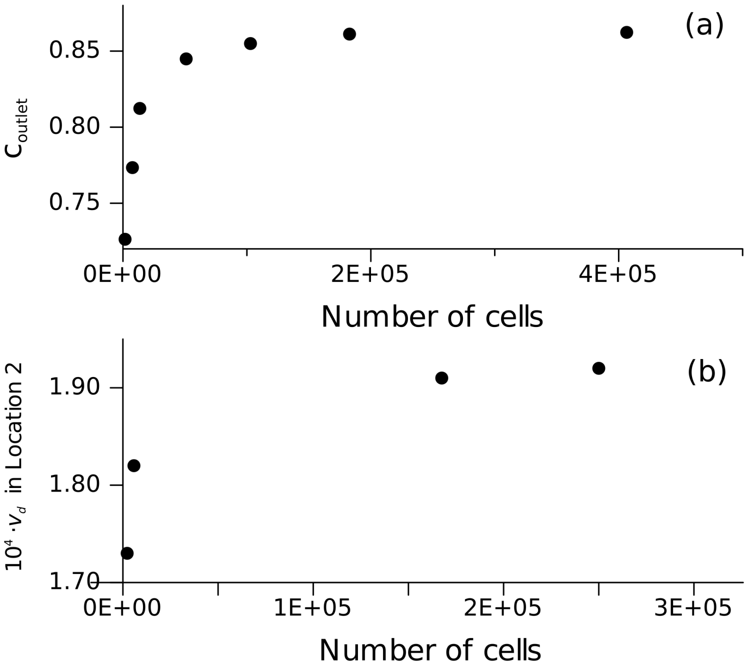

Figure 1: Grid independence test of the tunnel geometry (a) and the room case (b).

after a grid independence test, using the most sensitive variable in each case. In the case of the tunnel, this variable was the outlet concentration. The calculated concentration became independent of the grid size when cells were smaller than 0.5 cm. In the case of the room, the chosen variable was the deposition velocity in Location 2. This value became independent of the grid size at meshes smaller than 10 cm. These results are shown in Figure 1. The transient simulations were carried out with a 0.1 second time step and a first-order implicit formulation. The CPU time using a Intel Core i5-6200U Processor (3MB Cache, 2.80 GHz and 4GB RAM) was $\sim$ 15 minutes for steady-state simulations of the tunnel and the room, and $\sim$ 60 minutes for transient simulations.

7 Model validation in experimental tunnel

7.1 Experimental setup

We used an experimental tunnel with dimensions of 15 cm x 15 cm x 1.8 m, which is similar to the tunnel used by Lai et al. [41] to test the same model. In our tunnel, however, 10 internal barriers positioned every 13 cm generate gradients of velocity and increase the shear flow near certain horizontal surfaces. The dimensions of the barriers were 10 cm x 15 cm, leaving a free section of 5 cm x 15 cm. Air was displaced by a fan located at the outlet of the tunnel after a diffuser. We added a 45 cm buffer section with no barriers

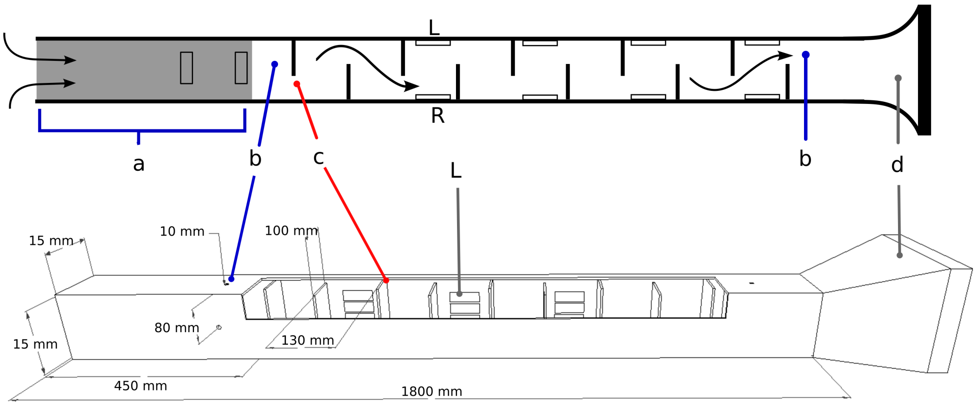

Figure 2: Diagram of the experimental tunnel showing the buffer area (a), the location of the condensation particle counters (b), the hot-wire anemometer (c) and the fan and diffuser system (d). R and L indicate the location of the right wall and left wall glass slides used to collect particles in the coarse PM deposition experiments.

before the experimental tunnel with the aim of ensuring that the introduced aerosol was distributed evenly through the section area. A schematic view and the dimensions of the experimental setup can be seen in Figure 2. We set a constant velocity of 0.25 ± 0.11 m/s at the inlet in all the experiments, which led to a maximum velocity of 0.76 ± 0.06 m/s in the gaps left by the barriers. Air velocity was measured at the inlet with a hot-wire anemometer, placed in the gap left by the first barrier. Particles were sampled at the inlet and outlet of the tunnel using two particle condensation counters (TSI P-Trak), which provided the number concentration of all particles in the size range $0.02 - 1$ μm.

The reported experiments took place indoors, in the Heritage Science Laboratory at UCL, London. This laboratory is located in a basement and is mechanically ventilated. The background concentration of $\mathrm{PM}_{0.02-1}$ was about $2000 - 4000$ $1/\mathrm{cm}^3$. Because the purpose of this research is to use the model to study actual heritage sites, we decided to use as input sources of aerosols common in heritage environments: resuspended dust, candle smoke and untreated air from the environment.

7.2 Data collection

We measured particle concentration at the inlet and outlet of the tunnel, as well as deposition fluxes on several surfaces. We carried out two types of experiment:

1. Experiments with suspended fine PM with particle diameter in the range of $0.02 - 1$ μm. We used two strategies to feed particles into the tunnel. The first was to direct a burst of a commercially available duster spray (Ambersil Air Duster, flow rate 0.5 g/s, density 1.21 kg/m^3) towards the neighboring

surfaces of the experimental area, causing uncontrolled dust resuspension. The second consisted in using the aerosol emitted by a burning candle. This was placed at the inlet section of the experimental tunnel for short periods of time (≤ 2 s).

2. Experiments with deposited coarse PM with particle diameter in the range of $0.5-10$ μm. In these experiments we let the tunnel collect air from its surroundings. This air displayed a variable aerosol concentration that fluctuated during the day. During 72 h we monitored the inlet number concentration continuously. We sampled the deposited particles using microscope glass slides (75 by 25 mm) placed inside the tunnel at the locations specified in Figure 2.

Our measurements of deposited PM were size-resolved, while the measurements of concentration focused on a single size fraction, particle diameter in the range between $0.02-1$ μm. As demonstrated by Zai et al. [58] and Li and Hopke [59], candle smoke has a typical particle size distribution with most particles being between 0.01 and 0.1 μm, which falls within the measured size range.

All the experiments were transient, *i.e.*, the inlet concentration varied over the course of the experiment. However, as we shall see, some of these experiments can be modeled via steady-state simulations. In the first set of experiments several concentration peaks of candle smoke or dust were produced while the inlet and outlet concentrations were continuously monitored with a frequency of 1 s during about 1 h. As can be seen in Figure 3, every concentration peak measured at the inlet undergoes a change within the tunnel, and emerges at the outlet displaying a smoother signal. We excluded the peaks that did not meet the following inclusion criteria from the experiment: inlet peaks should reach a maximum and decrease in no more than

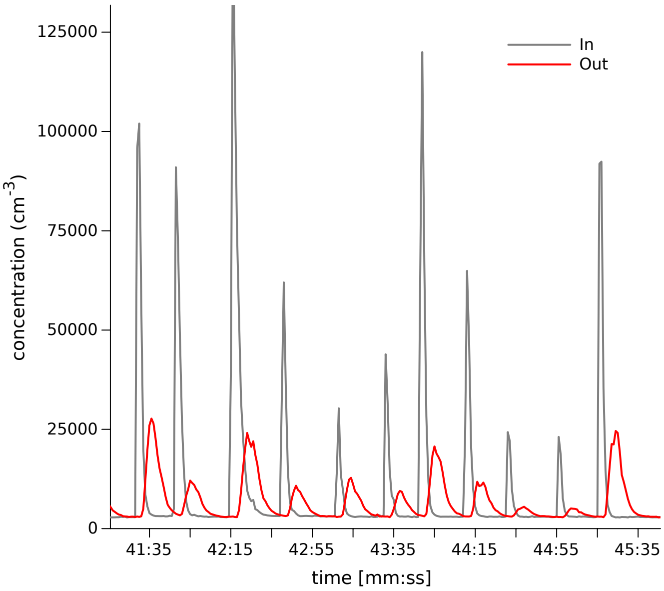

Figure 3: Example of inlet concentration peaks and their reflection in the outlet. Plot shows part of a 1 h experiment.

2 s (so that the peak can be idealized mathematically as a 1 s step), and they should not be higher than 10^6 $1/\mathrm{cm}^3$ (as a precaution to avoid coagulation).

In the second set of experiments we installed glass slides in four locations on the right (R_{1-4}) and left (L_{1-4}) walls of different compartments (the space between barriers). Slides in locations R_{1-4} were placed on walls adjacent to the gap left by the barriers, while slides L_{1-4} were placed just after a barrier. As a consequence, the air flowing next to the slides L_{1-4} and R_{1-4} had different levels of turbulence. In each location, we introduced three slides in order to obtain repeated measurements (the locations can be seen in Figure 2). We used a digital optical microscope to count the number of deposited particles on each slide, from which we obtained the deposition flux. This procedure is described in Annex 1.

7.3 Results and discussion

We observed that in the flow regime of operation and within the size range of interest, one size mode is enough to describe particle behavior. The assumption that particles can be characterized by an average diameter and density is reasonable in this case because, under the conditions of the experiment, these two variables have a very limited impact on the overall deposition flux. This can be demonstrated by comparison with similar cases in the literature and with an analytical solution of the deposition model.

Naturally, the small influence of the particle diameter is a property of the system, as often deposition depends strongly on particle size, particularly in environments with low air velocity. Particles close to the lower size range detected by our instrument ($d_s = 0.02$ μm) are affected by Brownian motion (characterized by the diffusivity $\mathscr{D}$) whereas deposition in the higher size range ($d_s = 1$ μm) is dominated by gravitational settling, represented by the terminal velocity $\boldsymbol{v}$ in Equation 3.1. However, as turbulence increases – *e.g.*, if a room is mechanically ventilated – turbulent diffusion becomes dominant and the differences of deposition owing to particle size are reduced over a large size range. This has been observed experimentally in small chambers. For example Lai and Chen [22] detected identical deposition rates for particles between 0.02 and 1 μm in a small chamber (100 liters) with an inlet velocity of 0.225 m/s. The deposition ratio of particles between 0.01 and 3 μm is also constant in some of the experiments reported in Lai [2], particularly those with high surface-to-volume ratios and high ventilation rates. Lai and Nazaroff [60] also observed similar deposition rates between 0.9 and 4 μm on vertical rough surfaces in a stirred chamber (1.8 m^3). In these cases, size differences are small, and deposition gradients are mainly controlled by the flow pattern.

This can be exemplified by a solution of Equation 3.2 in a single computational cell. The results are shown in Figure 4. The plot reported illustrates that deposition velocities are independent of the properties of the particles when $\mathscr{D}_t$ is orders of magnitude higher than Brownian diffusivity. The values of $\mathscr{D}_t$ reported

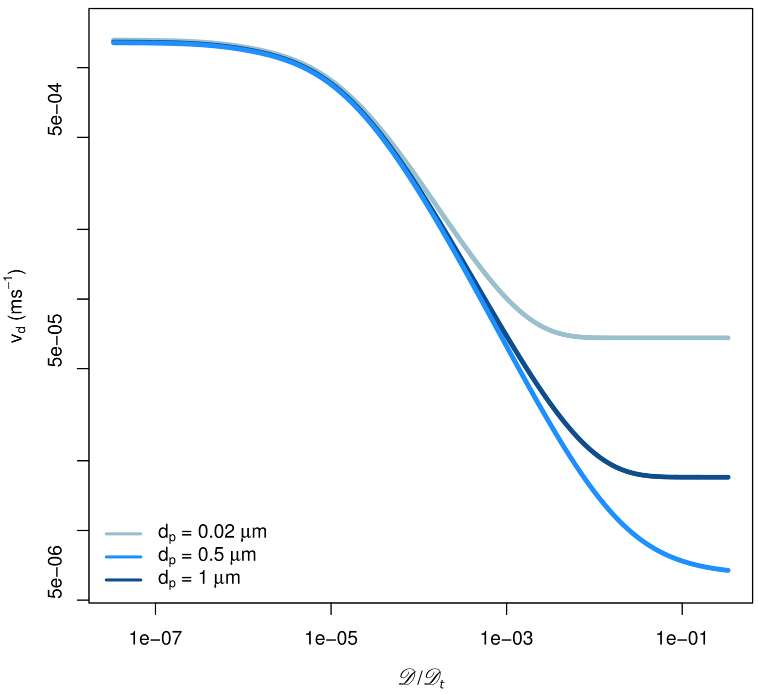

Figure 4: Deposition velocity in a single computational cell for different values of the turbulent diffusivity. The Brownian diffusivity of the particles is constant.

in Figure 7e range from 10^{-3} m^2/s to 10^{-4} m^2/s, while the Brownian diffusivity in our system is typically 10^{-10} m^2/s. This clearly indicates that our experiments operate in conditions where $\mathscr{D}/\mathscr{D}_t \lll 1$. So, under our experimental conditions the differences between the deposition velocities of different size modes are not significant, and simulating several particle sizes would be superfluous. In any case, this simplification does not affect the applicability of the drift-flux model, which could easily incorporate the simulation of different particle sizes, should this be required.

7.4 Suspended fine PM

The concentration of particles decays steadily through the length of the tunnel. Similar trends have been observed in studies of ventilation ducts with a comparable geometry [14]. In our system, $c_{\text{out}}/c_{\text{in}} = 0.86$. However, as shown in Figure 5, which reports the simulation results, the presence of the barriers causes a non-linear decay. The smoothing of the peaks observed in Figure 3 is caused by the combined effects of dispersion and deposition, both of which are independent of the total concentration. Consequently, when the concentration profiles at the outlet of the tunnel are normalized with the inlet concentration (taken as the highest value of the inlet peak), they conform to a common shape (Figure 6). This property makes

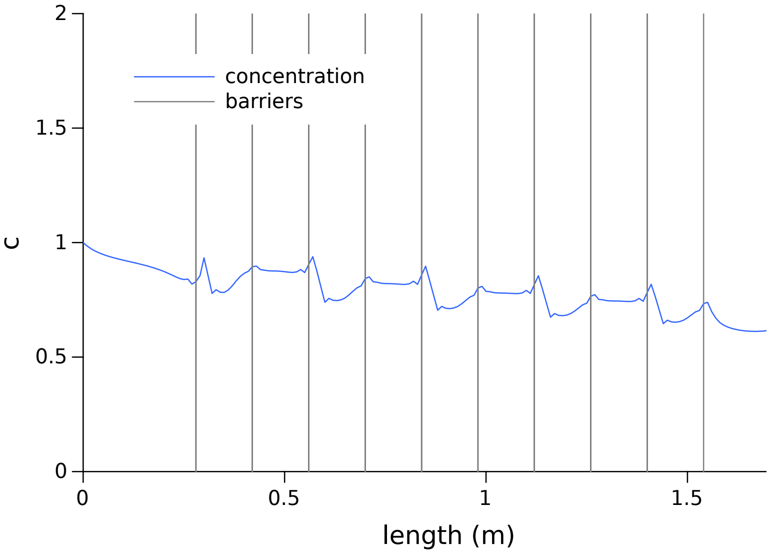

Figure 5: Example of the decay of concentration throughout the tunnel displaying a constant reduction of concentration. The horizontal lines show the position of the barriers. All the profile is realistic except for the concentration in the last few computational points, whose value is dictated by the outlet boundary condition.

the experiments highly repeatable and enables the combined assessment of two key aspects of the model: its accuracy in predicting particle deposition fluxes and its ability to reflect the diffusive dispersion of the particles through the tunnel.

The temporal variation of the concentration at the outlet of the tunnel, shown in Figure 6, was reproduced using a dynamic simulation. In this simulation the inlet velocity is $0.25\ \mathrm{m/s}$, the particle diameter is assumed to be the mean diameter in the measured size range ($0.5\ \mu\mathrm{m}$), and the density is assumed to be $1500\ \mathrm{kg/m^3}$. A peak of particles is created by setting a dimensionless particle concentration of one at the inlet during the first second of the simulation.

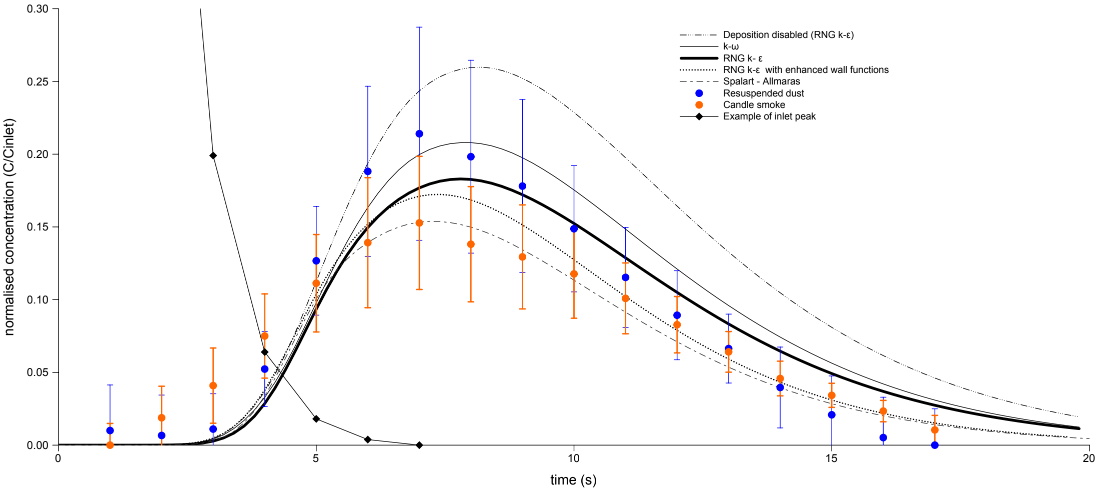

Figure 6: Normalized particle concentration profiles at the outlet of the tunnel and comparison with the CFD simulation results. The error bars indicate ±1 standard deviation.

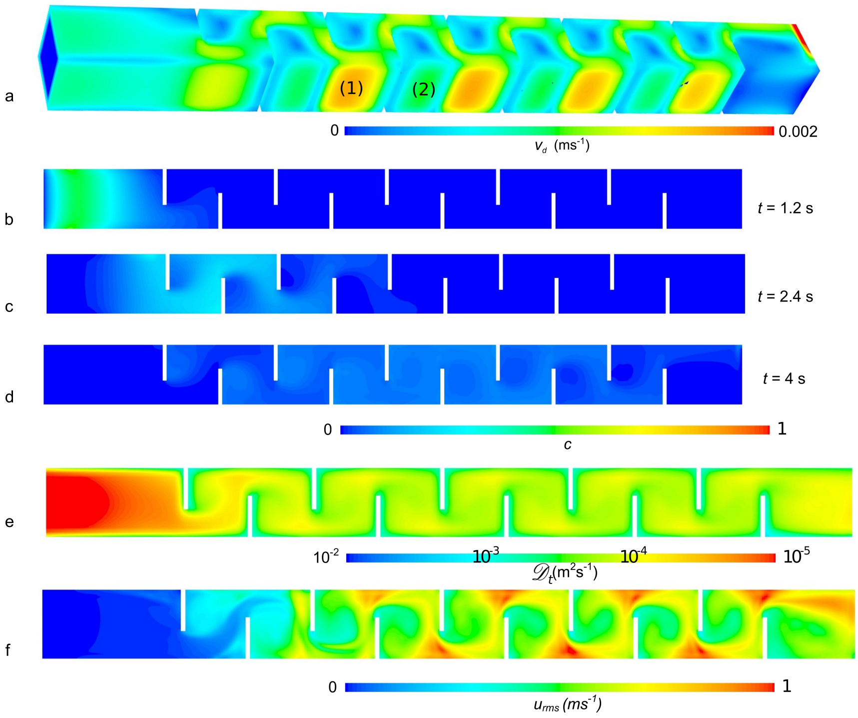

Figure 7: Contour images of several parameters from the simulations. From top to bottom: deposition velocity (a), three stills of the dynamic solution of the single peak experiment (b,c,d), turbulent diffusivity (e) and u_{rms} (f). In (a) contours are shown in the walls in perspective view, while the next images show the central sectional cut of the tube viewed from above. Locations (1) and (2) indicate the areas after a gap and after a wall respectively, which display different deposition velocities.

Figure 6 compares the experimental values of outlet concentration with the results obtained with different turbulence models (the data employed to produce Figure 6 are available in Annex 2). All the tested models (Spalart-Allmaras, $k-\omega$, RNG $k-\varepsilon$ and RNG $k-\varepsilon$ with enhanced wall functions) capture the non-trivial shape of the concentration peak. The $k-\omega$ model underestimates deposition; however, the results are within the experiment standard deviation for most of the peak. The RNG $k-\varepsilon$ model with enhanced wall functions seems to offer a better match with the decreasing slope, but it also seems to overestimate deposition slightly when it is compared with the resuspended dust curve. The Spalart-Allmaras model overestimates deposition quite clearly. The differences between candle smoke and resuspended dust are not statistically significant. The particles present in the tunnel before a time of about three seconds might correspond to pre-existing particles in the tunnel.

7.5 Deposited coarse PM

We also simulated the deposition of particles belonging to the background concentration adopting a single particle size (2.5 μm). In the contours of the simulated deposition velocity v_d (Figure 7a) we may observe that the deposition is always higher just before a barrier, as shown in location (1) of Figure 7a. This contrasts

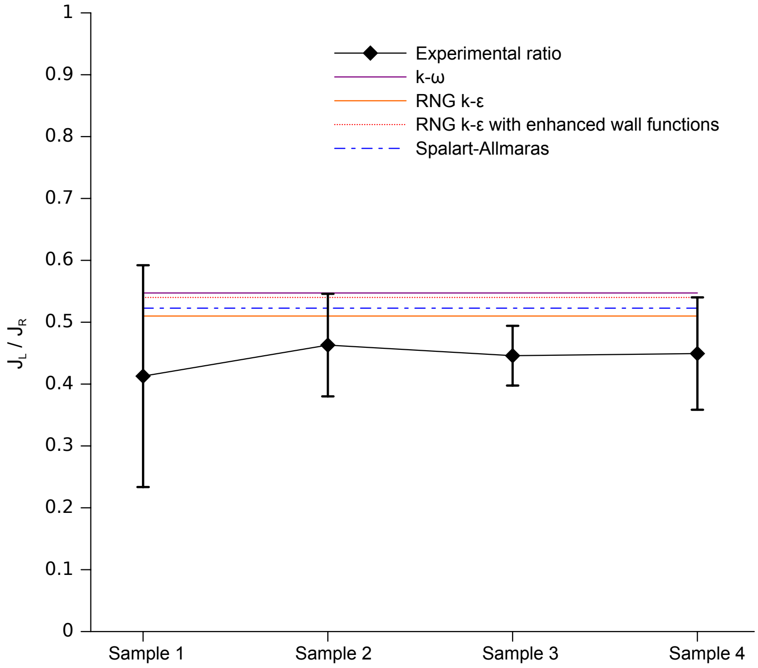

Figure 8: Experimentally determined values of the left-to-right ratio of deposition velocities ($J_{L,1-4}/J_{R,1-4}$) compared with the ratios predicted by different turbulence models. The samples of this Figure correspond with the locations indicated in Figure 2. The error bars indicate ±1 standard deviation.

with the deposition in straight tunnels, in which the flux toward all vertical walls is identical [14]. On the contrary, our tunnel displays marked differences between walls that are more or less exposed to the air flow.

This difference is a consequence of important features of the flow. We have observed that air in contact with the R_{1-4} samples displays a high velocity tangential to the wall that leads to increased wall shear stress, while $\mathscr{D}_t$ has a similar value near both sampling points (as seen in the diffusion contours of Figure 7e). τ_w is related to the deposition velocity through Equation 3.2. Therefore, it is natural to expect that deposition will be higher in the regions where higher values of τ_w are present.

We expressed the difference in deposition between left and right walls as the ratio of deposition fluxes, $\xi \equiv J_{L,1-4}/J_{R,1-4}$. This is constant during the experiment and independent of particle concentration; thus, it can be predicted by means of a steady-state simulation. The ratio has a mean value of $\xi_{\text{exp}} = 0.44 \pm 0.10$ across the tunnel if we calculate it for all particles between 0.5 and 5 μm (the size-resolved particle counts are available in Annex 3). This implies that deposition in areas where the direction of the velocity field is approximately parallel to the wall is twice as much as that in areas protected from air flow. The simulations give $\xi_{\text{sim}} = 0.51 \pm 0.12$ (Figure 8). The computed ratios systematically overestimate the deposition ratio by about 20%, but this error is within the standard deviation of the experiments. Also, no significant differences are observed between the values of ξ_{sim} predicted by the different turbulence models.

8 Simulation of an indoor heritage environment

8.1 Site description

The room we simulate is on the lower floor of Apsley House, London, a historical house managed by English Heritage. The room is furnished with glass cabinets that host a collection of porcelain which is prone to soiling by particulate matter. The staff has reported the accumulation of black deposits and that many surfaces require weekly cleaning. The House is located at Hyde Park Corner, a very busy roundabout. We have determined in previous research that a large fraction of fine outdoor particles penetrate into the building, mainly through the leaks in the windows of the south and west façades [61].

We monitored PM deposition in the room between January and June 2013. We counted the deposited particles every month adopting the same method described in Annex 1, in the sampling locations shown in Figure 9. Locations 1 and 2 are on top of the display cabinets, while locations 3 and 4 are on their walls. For this analysis we used particle counts in the size range $0.5-2.5$ μm. We measured the concentration of suspended particles in this size range with an optical particle counter (DC1100, Gradko, UK) over the experimental period. The average indoor concentration of these particles was $1.15 \pm 0.74 \cdot 10^6$ $1/\text{m}^3$, with an average I/O ratio of 0.67 ± 0.37. The geometry of the room is illustrated in Figure 9. Structurally, the system is ostensibly different from the tunnel described in the previous section. There are, however, some common features. The air inlets are placed close to the display cabinets, resulting in forced convection and, as a consequence, in areas of increased tangential velocities, as those emulated in the tunnel. In both cases

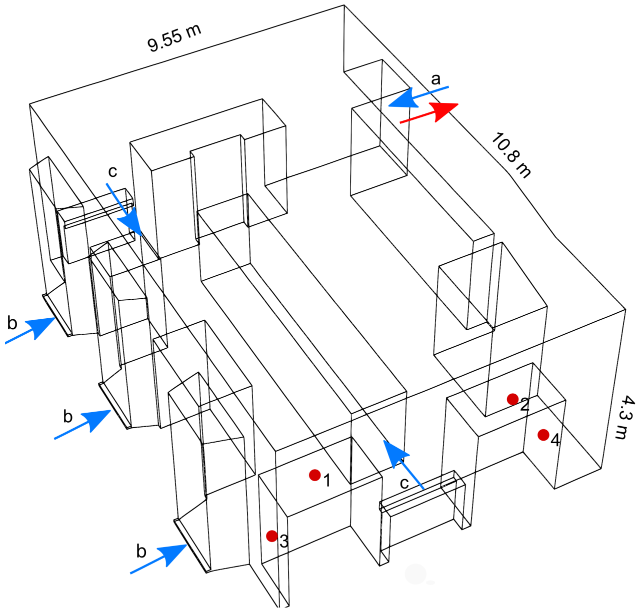

Figure 9: Schematic view of the simulated room. (a) main door, (b) leakage inlets, one in each window, (c) ventilation inlets. Monitoring locations 1 and 2 are on top of display cases, and 3 and 4 on the side.

deposition is caused by a boundary layer turbulent flow. The air velocity is of the same order of magnitude. The main difference between the two systems is that in the wall bounded flow the near-wall layers have a constant thickness, while they grow constantly in the unbounded flow. Nevertheless, deposition is caused by the near-wall turbulence, which exists in both cases, since near-wall turbulence arises as long as the flow is turbulent and parallel to a wall.

Most importantly, the dimensionless numbers characterizing the systems (summarized in Table 1) are comparable: in both cases, K_{pt} is very small, and therefore one can assume that $\mathscr{D}_t = \nu_t$. Moreover, in all cases, $\mathscr{D}/\mathscr{D}_t \ll 1$, which suggests that particle transport is dominated by the turbulent diffusivity.

	Tunnel	Room Case A	Room Case B	Room Case C
K_{pt}	$4.09 \cdot 10^{-4}$	$5.64 \cdot 10^{-10}$	$1.12 \cdot 10^{-6}$	$7.33 \cdot 10^{-7}$
$\mathscr{D}/\mathscr{D}_t$	$4.92 \cdot 10^{-8}$	$4.72 \cdot 10^{-5}$	$2.78 \cdot 10^{-8}$	$2.54 \cdot 10^{-8}$

Table 1: Average value of some non-dimensional parameters of the simulated cases. The values correspond to simulations with $d_s = 0.5$ μm.

The room operates as follows. It has three windows with leaks that are sources of fine particles (Figure 9). It is also equipped with a ventilation system which is operated intermittently by the staff. It has a single door, which is an inlet or an outlet of air depending on the wind direction. If the latter is South-West [which is the predominant scenario, roughly 75% of the six-month experimental period [61]], we have observed that the door acts as an outlet of air and the leaks as an inlet. This set of sources leads to several possible operation scenarios, of which we consider the following:

1. South-West wind, leakage, the ventilation system is off and the door is an outlet. This is the most common scenario during the year.
2. South-West wind, leakage, the ventilation system is on and the door is an outlet. It is the second most likely scenario.
3. North-East wind, no leakage, the ventilation system is on and the door is an inlet. Albeit uncommon, we add this scenario for comparison.

The primary concern of the house managers is first to know which of these scenarios results into increased particle deposition and second to determine which areas of the room should be avoided for the display of valuable objects.

	A			B			C		
Boundary	c	u	Type	c	u	Type	c	u	Type
Main door	0.5	-	O	0.5	-	O	0.5	0.1	I
Ventilation	0.0	-	W	0.0	0.5	I	0.0	0.5	I
Leakage	1.0	0.001	I	1.0	0.001	I	1.0	-	W

Table 2: Simulation setup and boundary conditions. u is in $\mathrm{m/s}$. W is a wall, O is an outlet and I is an inlet.

To simulate these three scenarios, we translated them into a set of boundary conditions. We determined the concentration and velocity in the leaks in Grau-Bove et al. [61]. The boundary conditions for each scenario are summarized in Table 2.

8.2 Results and discussion

For this simulation we used two types of particles, coarse ($d_s = 10$ μm) and fine ($d_s = 0.5$ μm), with a density of 1500 $\mathrm{kg/m^3}$. Contrary to the tunnel experiment, deposition in some scenarios is dependent on particle properties, and therefore cannot be simulated with a single size mode. As we shall see, this is due to lower turbulent intensities in absence of forced ventilation. For this reason, we choose the particle sizes for which concentration and deposition data were available.

The simulations reveal marked differences between the cases with and without ventilation. Figure 10 displays the contours of air velocity and deposition velocity for the coarse and fine particles. Notice that, when the ventilation system is off (Case A), the deposition velocity v_d is different for the two particle sizes. Coarse particles tend to deposit in upward-facing surfaces, while fine particles deposit more homogeneously. As shown in Table 1, the ratio between Brownian and turbulent diffusion for the smallest particles ($\mathscr{D}/\mathscr{D}_t$) is the largest of all cases. Its average value is $4.72 \cdot 10^{-5}$ (and its maximum value is $1.40 \cdot 10^{-3}$), and therefore falls within the region of Figure 4 where size differences become significant. Furthermore, since deposition is controlled by gravitational settling, it is similar on all the upward-facing horizontal surfaces.

The situation changes significantly when the ventilation system operates (cases B and C). Firstly, there is a global increase in air motion which results in higher turbulent diffusivity. In consequence, the values of $\mathscr{D}/\mathscr{D}_t$ in Cases B and C are comparable to those observed in the tunnel (that is, close to about 10^{-8}), which implies that due to the turbulence generated by the ventilation system all particles behave similarly. Secondly, turbulent boundary layers are formed on the vertical surfaces close to the ventilation outlets. This results in a local increase of the deposition velocity owing to shear stresses. This is the same phenomenon observed in the experimental tunnel, where shear flows result in a difference of deposition between the left

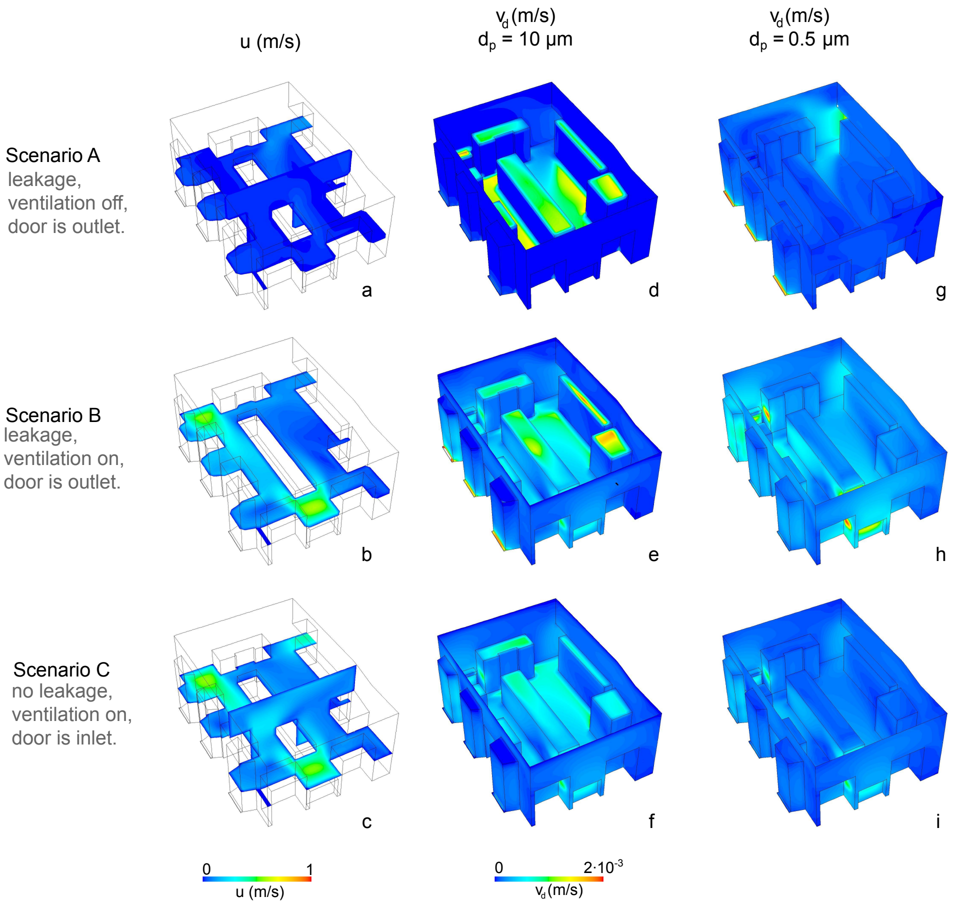

Figure 10: Contours of air velocity and deposition velocity in the simulated scenarios.

and right walls of the system. These hotspots of deposition are easily seen in Figures 10e, 10h, 10f and 10g. In some instances, this effect is slightly more marked for the fine particles.

While the contours of deposition of the different scenarios are remarkably diverse, the room is well-mixed and exhibits a homogeneous concentration, as seen in the contour of concentration displayed in Figure 11. The simulated values of c displayed in Figure 11 correspond to scenario A. Note that, as expected, the contours of c are almost uniform.

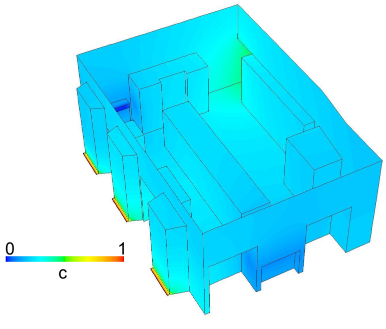

Figure 11: Contour of non-dimensional concentration corresponding with scenario A.

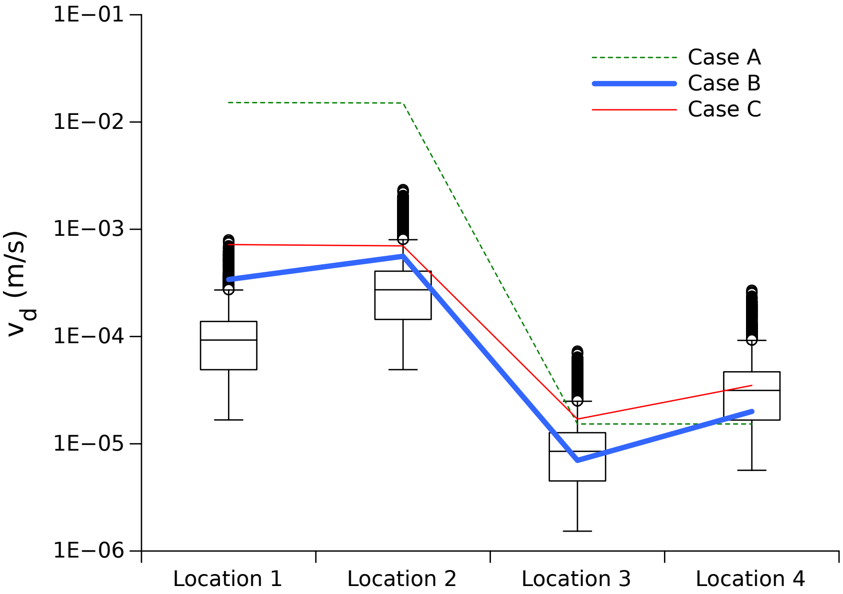

Figure 12: Comparison between predicted and measured deposition velocities in the four monitoring locations of the room. The box-plots show the experimental value, and indicate the distribution of deposition velocities related to the variation of c during the six-month monitoring period. The box indicates the first and third quartiles, and the whiskers the 2$^{\text{nd}}$ and 98$^{\text{th}}$ percentiles.

About the value of K_{pt}, the maximum value in all cases is vanishingly small. In all the cases studied we consider the assumption of $\mathscr{D}_t = \nu_t$ to be applicable. Under the current air flow conditions, this assumption would only become unreasonable (*i.e.*, K_{pt} would become much larger than unity) for values of the particle diameter of about 250 μm or larger.

We compared the simulated deposition velocities of the 0.5 μm particles with the deposition velocities calculated from our measurements (which we obtained employing the particle counts as well as the values of suspended PM concentration, see Annex 1). Figure 12 shows this comparison. The box-plots in Figure 12 reflect the variation of concentration during the monitoring period. Because the flux J was measured by counting the deposition on glass slides, it is not subject to any experimental error. Consequently, all the uncertainty in the estimation of the deposition velocity originates in the variation of c, which translates into a distribution of values for the deposition velocity v_d.

The simulations of scenarios B and C reflect quite well the differences of deposition velocity observed experimentally. In case A, conversely, the deposition on top of the display cases (locations 1 and 2) is greatly overestimated by the simulations. The simulations that coincide with the experimental measurements are those that involve the ventilation system. Interestingly, the largest values of deposition are observed in the scenario with no ventilation, on the top of the display cabinets. A possible explanation is that the increased air motion partially counteracts gravitational settling, when at the same time render deposition more even.

This implies that, when ventilation is on, air motion not only increases deposition on vertical surfaces, but slightly reduces deposition on horizontal upward-facing surfaces. Even though the ventilation system was only operated occasionally during the monitoring period, a total absence of air motion does not correspond well with the reality of the environment. If the simulations are correct, they indicate that some air movement is necessary (and was present) to explain the observed patterns of deposition, and that the actual air flow pattern might be similar to that of scenarios B and C. The available data do not suffice, however, to quantify the contribution of each scenario toward the total observed deposition.

Finally, this case illustrates that deposition fluxes and particle concentration are often independent of one another in indoor environments. In other words, the observed variations in the deposition velocity are of many orders of magnitude in a space which has an otherwise homogeneous concentration of airborne PM. It is clear that, from the perspective of deposition rates, the room is anything but well-mixed.

9 Conclusions

Research studies reported in the literature have shown the capability of the drift-flux model to account for deposition in well-mixed environments of a wide range of geometries, where deposition can be characterized by the overall decay rate of particle concentration. Our experiments show that this conclusion is extendable to environments with marked gradients of air velocity which result in inhomogeneous deposition. We have adopted the drift-flux approach to estimate the spatial distribution of deposition caused by shear flows in a tunnel and a large ventilated room. In the first system, the model successfully predicted the differences of deposition on walls affected by different degrees of near-wall turbulence. In the room, we have simulated three plausible scenarios, of which two provided estimations that coincide with the experimental data. But the scenario that reflects the most common setup of the room (*e.g.*, no mechanical ventilation) overestimated deposition on horizontal surfaces. The simulations of the room illustrate the importance of the definition of the boundary conditions when simulating complex and changeable environments. Care must be taken to identify boundary conditions that reflect the average behavior of a building during a period of time, which may not always be possible.

The two simulated systems can be regarded as very dilute multiphase systems (*i.e.*, systems with low aerosol volume fraction and low phase-mass ratio) of inertia-less particles (that is, $\mathrm{St} \ll 1$). These systems were successfully modeled with the one-way coupling modeling approach in an Eulerian framework. Both systems presented very low values of K_{pt}, the parameter that describes the ability of the particles to follow the fluid phase in turbulent eddies. In both systems, we assumed that $\mathscr{D}_t = \nu_t$. However, further research is needed to establish whether K_{pt} can be used as the sole indicator of the applicability of this assumption in indoor aerosol deposition studies.

The experiments and simulations show the importance of local air flow patterns in the deposition flux. We have seen that deposition is increased in areas that experience high shear stress, both in the tunnel and in the real room. These observations suggest that, in heritage settings, the display of objects on surfaces close to air inlets and outlets should be avoided. The results also highlight that when turbulence is high (*i.e.*, when $\mathscr{D}/\mathscr{D}_t \ll 1$ and convection is less important than diffusion), the differences between particles become less significant, and therefore many situations can be implemented with a single particle size. This suggests a great applicability of the drift-flux approach in situations with unknown particle properties, for example as an exploratory tool for heritage institutions without access to aerosol monitoring equipment. Even though this is a convenient simplification, its applicability must be assessed on a case-by-case basis, as a strong dependence of deposition rates on particle size has been repeatedly observed in many different situations. As we have seen in the room simulations, this ceases to be true when air is steady, which is common in indoor environments.

Acknowledgements

The authors would like to thank Tom Fearn for his advice on statistical analysis and Dejan Mumovic and David Thickett for allowing us to use indispensable experimental equipment. Also, special thanks should go to Mark Underhill for his patience and continued help, and to Joan Fuster for his theoretical support.

References

[1] C. Kleinstreuer, Z. Zhang, Airflow and particle transport in the human respiratory system, Annual Review of Fluid Mechanics 42 (2010) 301–334.

[2] A. C. K. Lai, Particle deposition indoors: a review, Indoor Air 12 (2002) 211–214.

[3] J. Grau-Bove, M. Strlic, Fine particulate matter in indoor cultural heritage: a literature review, Heritage Science 1 (2013) 8.

[4] W. Anaf, L. Bencs, R. V. Grieken, K. Janssens, K. D. Wael, Indoor particulate matter in four belgian heritage sites: Case studies on the deposition of dark-colored and hygroscopic particles, Science of The Total Environment 506-507 (2015) 361–368.

[5] D. Camuffo, Wall temperature and the soiling of murals, Museum Management and Curatorship 10 (1991) 373–383.

[6] J. Grau-Bove, L. Mazzei, D. Thickett, L. Malki-Ephstein, M. Strlic, CFD simulation of aerosol deposition in apsley house, london, in: Proceedings of the 14th Conference on Building Simulation and Optimization., London, UK, 2014.

[7] B. Zhao, J. Wu, Particle deposition in indoor environments: Analysis of influencing factors, Journal of Hazardous Materials 147 (2007) 439 – 448.

[8] A. C. K. Lai, W. W. Nazaroff, Modeling Indoor Particle Deposition From Turbulent Flow Onto Smooth Surfaces, Journal of Aerosol Science 31 (2000) 463–476.

[9] F. Chen, S. Yu, A. C. K. Lai, Modeling particle distribution and deposition in indoor environments with a new drift–flux model, Atmospheric Environment 40 (2006) 357–367.

[10] N. Gao, J. Niu, Modeling particle dispersion and deposition in indoor environments, Atmospheric Environment 41 (2007) 3862 – 3876.

[11] P. W. Longest, M. J. Oldham, Numerical and experimental deposition of fine respiratory aerosols: Development of a two-phase drift flux model with near-wall velocity corrections, Journal of Aerosol Science 39 (2008) 48 – 70.

[12] S. Parker, J. Nally, T. Foat, S. Preston, Refinement and testing of the drift-flux model for indoor aerosol dispersion and deposition modelling, Journal of Aerosol Science 41 (2010) 921 – 934.

[13] B. Zhao, C. Chen, Z. Tan, Modeling of ultrafine particle dispersion in indoor environments with an improved drift flux model, Journal of Aerosol Science 40 (2009) 29 – 43.

[14] B. Zhao, J. Wu, Modeling particle deposition from fully developed turbulent flow in ventilation duct, Atmospheric Environment 40 (2006) 457 – 466.

[15] S. Ramechecandane, C. Beghein, F. Allard, Modeling fine particle dispersion in an inhomogeneous electric field with a modified drift flux model, Building and Environment 45 (2010) 1536 – 1549.

[16] Z. Bin, L. Xianting, Z. Zhao, Numerical study of particle deposition in two differently ventilated rooms, Indoor and Built Environment 13 (2004) 443–451.

[17] C. Tsang-Jung, H. Ting-Shing, Transport mechanisms of airborne particulate matters in partitioned indoor environment, Building and Environment 43 (2008) 886 – 895.

[18] N. Gao, J. Niu, M. Perino, P. Heiselberg, The airborne transmission of infection between flats in high-rise residential buildings: Particle simulation, Building and Environment 44 (2009) 402 – 410.

[19] N. Gao, J. Niu, Transient cfd simulation of the respiration process and inter-person exposure assessment, Building and Environment 41 (2006) 1214 – 1222.

[20] S. Holmberg, Y. Li, Modelling of the indoor environment – particle dispersion and deposition, Indoor Air 8 (1998) 113–122.

[21] H. Qian, Y. Li, Removal of exhaled particles by ventilation and deposition in a multibed airborne infection isolation room, Indoor Air 20 (2010) 284–297.

[22] A. C. K. Lai, F. Chen, Modeling particle deposition and distribution in a chamber with a two-equation reynolds-averaged navier–stokes model, Journal of Aerosol Science 37 (2006) 1770 – 1780.

[23] M. Delele, A. Schenk, E. Tijskens, H. Ramon, B. Nicolai, P. Verboven, Optimization of the humidification of cold stores by pressurized water atomizers based on a multiscale CFD model, Journal of Food Engineering 91 (2009) 228 – 239.

[24] Z. Zhang, X. Chen, S. Mazumdar, T. Zhang, Q. Chen, Experimental and numerical investigation of airflow and contaminant transport in an airliner cabin mockup, Building and Environment 44 (2009) 85 – 94.

[25] D. Karadimou, N. Markatos, A novel flow-oriented discretization scheme for reducing false diffusion in three-dimensional (3d) flows: An application in the indoor environment, Atmospheric Environment 61 (2012) 327 – 339.

[26] D. P. Karadimou, N. C. Markatos, Modelling of two-phase, transient airflow and particles distribution in the indoor environment by large eddy simulation, Journal of Turbulence 17 (2016) 216–236.

[27] L. Ding, A. Lai, An efficient lattice boltzmann model for indoor airflow and particle transport, Journal of Aerosol Science 63 (2013) 10 – 24.

[28] H. Sajjadi, M. Salmanzadeh, G. Ahmadi, S. Jafari, Simulations of indoor airflow and particle dispersion and deposition by the lattice boltzmann method using LES and RANS approaches, Building and Environment 102 (2016) 1 – 12.

[29] Z. Tong, Y. Chen, A. Malkawi, G. Adamkiewicz, J. Spengler, Quantifying the impact of traffic-related air pollution on the indoor air quality of a naturally ventilated building, Environment International 89–90 (2016) 138 – 146.

[30] G. Stavrakakis, D. Karadimou, P. Zervas, H. Sarimveis, N. Markatos, Selection of window sizes for optimizing occupational comfort and hygiene based on computational fluid dynamics and neural networks, Building and Environment 46 (2011) 298 – 314.

[31] R. Ramponi, B. Blocken, CFD simulation of cross-ventilation for a generic isolated building: Impact of computational parameters, Building and Environment 53 (2012) 34 – 48.

[32] Z. Feng, Z. Long, Q. Chen, Assessment of various cfd models for predicting airflow and pressure drop through pleated filter system, Building and Environment 75 (2014) 132 – 141.

[33] Y. Tang, B. Guo, D. Ranjan, Numerical simulation of aerosol deposition from turbulent flows using three-dimensional rans and les turbulence models, Engineering Applications of Computational Fluid Mechanics 9 (2015) 174–186.

[34] B. Zhao, J. Wu, Effect of particle spatial distribution on particle deposition in ventilation rooms, Journal of Hazardous Materials 170 (2009) 449 – 456.

[35] L. Gidhagen, C. Johansson, J. Strom, A. Kristensson, E. Swietlicki, L. Pirjola, H.-C. Hansson, Model simulation of ultrafine particles inside a road tunnel, Atmospheric Environment 37 (2003) 2023 – 2036.

[36] A. C. K. Lai, Y. Ho, Spatial concentration variation of cooking-emitted particles in a residential kitchen, Building and Environment 43 (2008) 871 – 876.

[37] Z. Zhang, Q. Chen, Experimental measurements and numerical simulations of particle transport and distribution in ventilated rooms, Atmospheric Environment 40 (2006) 3396 – 3408.

[38] L. Wong, W. Chan, K. Mui, A. K. Lai, An experimental and numerical study on deposition of bioaerosols in a scaled chamber, Aerosol Science and Technology 44 (2010) 117–128.

[39] M.-F. King, C. Noakes, P. Sleigh, M. Camargo-Valero, Bioaerosol deposition in single and two-bed hospital rooms: A numerical and experimental study, Building and Environment 59 (2013) 436 – 447.

[40] J. Xi, P. W. Longest, Numerical predictions of submicrometer aerosol deposition in the nasal cavity using a novel drift flux approach, International Journal of Heat and Mass Transfer 51 (2008) 5562 – 5577. Biomedical-Related Special Issue.

[41] A. Lai, M. A. Byrne, A. Goddard, Aerosol deposition in turbulent channel flow on a regular array of three-dimensional roughness elements, Journal of Aerosol Science 32 (2001) 121 – 137.

[42] A. C. Lai, F. Chen, Comparison of a new eulerian model with a modified lagrangian approach for particle distribution and deposition indoors, Atmospheric Environment 41 (2007) 5249 – 5256. Indoor Air 2005 - 10th International Conference on Indoor Air Quality and Climate (Part II).

[43] A. Lai, F. Chen, Modeling of cooking-emitted particle dispersion and deposition in a residential flat: A real room application, Building and Environment 42 (2007) 3253 – 3260.

[44] D. Marchisio, R. Fox, Computational Models for Polydisperse Particulate and Multiphase Systems, Cambridge Series in Chemical Engineering, Cambridge University Press, 2013.

[45] S. Parker, T. Foat, S. Preston, Towards quantitative prediction of aerosol deposition from turbulent flows, Journal of Aerosol Science 39 (2008) 99–112.

[46] L. Gibilaro, Fluidization Dynamics, Elsevier Science, 2001.

[47] P. Reist, Aerosol science and technology, McGraw-Hill, 1993.

[48] B. Launder, D. Spalding, The numerical computation of turbulent flows, Computer Methods in Applied Mechanics and Engineering 3 (1974) 269 – 289.

[49] P. Huang, P. Bradshaw, T. Coakley, Skin friction and velocity profile family for compressible turbulentboundary layers, AIAA Journal 31 (1993) 1600–1607.

[50] F. White, G. Christoph, A Simple New Analysis of Compressible Turbulent Two-Dimensional Skin Friction Under Arbitrary Conditions, Defense Technical Information Center, 1971.

[51] A. Bush, Perturbation Methods for Engineers and Scientists, CRC Press library of engineering mathematics, Taylor & Francis, 1992.

[52] C. Lin, L. Segel, Mathematics Applied to Deterministic Problems in the Natural Sciences, Classics in Applied Mathematics, Society for Industrial and Applied Mathematics (SIAM, Philadelphia), 1988.

[53] R. Kohli, K. Mittal, Developments in Surface Contamination and Cleaning - Methods for Removal of Particle Contaminants, Developments in surface contamination and cleaning, Elsevier Science, 2011.

[54] M. Schnell, C. Cheung, C. Leung, Investigation on the coagulation and deposition of combustion particles in an enclosed chamber with and without stirring, Journal of Aerosol Science 37 (2006) 1581–1595.

[55] A. Dewan, Tackling Turbulent Flows in Engineering, Springer, 2010.

[56] L. Glasgow, Transport Phenomena: An Introduction to Advanced Topics, Wiley, 2010.

[57] FLUENT, FLUENT 6.3 User's Guide, Fluent Inc., 2006.

[58] S. Zai, H. Zhen, W. Jia-Song, Studies on the size distribution, number and mass emission factors of candle particles characterized by modes of burning, Journal of Aerosol Science 37 (2006) 1484 – 1496.

[59] W. Li, P. K. Hopke, Initial size distributions and hygroscopicity of indoor combustion aerosol particles, Aerosol Science and Technology 19 (1993) 305–316.

[60] A. C. K. Lai, W. Nazaroff, Supermicron particle deposition from turbulent chamber flow onto smooth and rough vertical surfaces, Atmospheric Environment 39 (2005) 4893 – 4900.

[61] J. Grau-Bove, L. Mazzei, L. Malkii-Ephstein, D. Thickett, M. Strlic, Simulation of particulate matter ingress, dispersion and deposition in a historical building, Journal of Cultural Heritage 18 (2016) 199 – 208.

Annex 1

After exposure, the glass slides were photographed with an optical microscope. Approximately ten images of every sample were taken. We used a magnification that provided a pixel size of 0.13 μm. However, we did not count particles smaller than four pixels, to avoid an overestimation of the amount of fine particles. With this setup, the smallest particles that could be measured had a diameter of about 0.3 μm, which is close to the theoretical minimum detectable by the naked eye, which is given by the wavelength of the visible light (390 nm).

The particles were counted with a combination of open source software, using *ImageJ* for image post-processing and particle counting, and the statistical software R for data analysis. This process was automated with macros. Particle deposition fluxes were calculated for every particle size as:

$$J_{\text{experimental}} = \frac{N_i}{At} \tag{9.1}$$

where N_i is the total number of particles of size i counted on the sampled surface, t is the exposure time (the duration of the experiment) and A is the area of the sampled surface.

The open source application *imagemagick* was used to prepare the images for post-processing, firstly converting images from gray-scale to binary black-and-white, with an adjustable threshold of luminosity. A square section was cut in the center of every image to avoid false readings from the peripheral areas out of focus.

```
%
mogrify -threshold 30% -gravity Center
-crop 3000x3000+0+0 *.TIFF
%
```

Then an *ImageJ* macro was applied to the images. The macro smoothed the contours of the image, thus eliminating any image noise pixels that could be counted erroneously as particles. Then particles were analyzed, leaving out any particle smaller than two pixels and accepting particles of any circularity. A list of particle sizes (measured in areas) was saved in text files that were later read and processed with R.

```
%
dir = getDirectory("image");
 name=getTitle;
 path = dir+name;

run("Smooth");
run("Smooth");
run("Smooth");

run("Make Binary");
run("Analyze Particles...",
    "size=2-Infinity
         circularity=0.00-1.00
        show=Nothing
        display exclude
        clear include
        summarize record");
saveAs("Text", path);
%
```

The raw data obtained with this procedure are in particle counts per 30 days. To enable a comparison with the simulated results (which are displayed in terms of deposition velocity), we converted particle counts into deposition velocities, $v_{d,\text{exp}}$, using the following relation:

$$v_{d,\text{exp}} = \frac{N}{At} \cdot \frac{1}{c} \tag{9.2}$$

where N is the total particle number, A is the area of the surface on which the particles were counted, t is the elapsed time (a month in seconds) and c is the number concentration of particles surrounding the deposition sampler.

Annex 2

The attached file *data.xlsx* contains the concentration curves used to produce Figure 6.

Annex 3

Figure 13 shows the distribution of particulate matter on measured on the glass slides location on the left and the right walls of the experimental tunnel. It demonstrates that most of the particles are smaller than 5 μm. It also shows clearly that the amount of measured particles is higher in the right walls of each compartment, as expressed quantitatively in Figure 8.

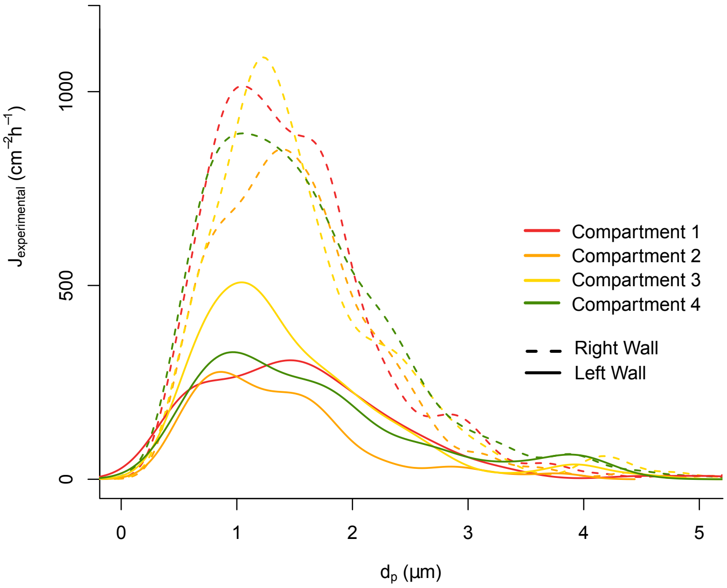

Figure 13: Size-resolved particle counts on the left and right walls of the tunnel. The data displayed in this figure was used to calculate the left-to-right ratio ξ displayed in Figure 8.